The Astrophysical Journal, 791:21 (15pp), 2014 August 10 doi:10.1088/0004-637X/791/1/21

FOURIER ANALYSIS OF BLAZAR VARIABILITY

Justin D. Finke[1] and Peter A. Becker[2]
[1] U.S. Naval Research Laboratory, Code 7653, 4555 Overlook Avenue SW, Washington, DC 20375-5352, USA; justin.finke@nrl.navy.mil
[2] School of Physics, Astronomy, and Computational Sciences, MS 5C3, George Mason University, 4400 University Drive, Fairfax, VA 22030, USA
Received 2014 February 12; accepted 2014 June 5; published 2014 July 22

ABSTRACT

Blazars display strong variability on multiple timescales and in multiple radiation bands. Their variability is often characterized by power spectral densities (PSDs) and time lags plotted as functions of the Fourier frequency. We develop a new theoretical model based on the analysis of the electron transport (continuity) equation, carried out in the Fourier domain. The continuity equation includes electron cooling and escape, and a derivation of the emission properties includes light travel time effects associated with a radiating blob in a relativistic jet. The model successfully reproduces the general shapes of the observed PSDs and predicts specific PSD and time lag behaviors associated with variability in the synchrotron, synchrotron self-Compton, and external Compton emission components, from submillimeter to γ-rays. We discuss applications to BL Lacertae objects and to flat-spectrum radio quasars (FSRQs), where there are hints that some of the predicted features have already been observed. We also find that FSRQs should have steeper γ-ray PSD power-law indices than BL Lac objects at Fourier frequencies $\lesssim 10^{-4}$ Hz, in qualitative agreement with previously reported observations by the *Fermi* Large Area Telescope.

Key words: BL Lacertae objects: general – galaxies: active – galaxies: jets – quasars: general – radiation mechanisms: non-thermal

Online-only material: color figures

1. INTRODUCTION

Blazars, active galactic nuclei (AGNs) with jets moving at relativistic speeds aligned with our line of sight, are the most plentiful of the identified point sources observed by the *Fermi* Large Area Telescope (LAT; Abdo et al. 2010b; Nolan et al. 2012). Their spectral energy distributions (SEDs) are dominated by two components. At lower frequencies there is a component produced via synchrotron emission, peaking in the radio through X-rays. There is also a high-energy component in γ-rays, most likely due to Compton-scattered emission. The seed photons for Compton scattering could be the synchrotron photons themselves (synchrotron self-Compton or SSC; Bloom & Marscher 1996), or they could be produced outside the jet (external Compton or EC) by the accretion disk (Dermer & Schlickeiser 1993, 2002), the broad-line region (Sikora et al. 1994), or a dust torus (Kataoka et al. 1999; Błażejowski et al. 2000). The Doppler boosting due to the combination of relativistic speed and a small jet inclination angle amplifies the observed flux, shifting the emission to higher frequencies, and decreasing the variability timescale.

The LAT monitors the entire sky in high-energy γ-rays every 3 hr, providing well-sampled light curves of blazars on long timescales. For some sources, γ-ray data have been supplemented by high cadence observations in the radio through very high energy (VHE) γ-rays creating unprecedented light curves with few gaps in wavelength or time (e.g., Abdo et al. 2011b, 2011c). Blazar variability is often characterized by power spectral densities (PSDs; e.g., Abdo et al. 2010c; Chatterjee et al. 2012; Hayashida et al. 2012; Nakagawa & Mori 2013; Sobolewska et al. 2014), which are essentially representations of the Fourier transform without phase information. Although the LAT can provide long baseline, high cadence light curves, it has difficulty probing short timescales for all but the brightest flares. However, shorter-timescale variability may be observed with optical, X-ray, or VHE instruments (e.g., Zhang et al. 1999, 2002; Kataoka et al. 2001; Cui 2004; Aharonian et al. 2007; Rani et al. 2010). Less often, Fourier frequency-dependent time lags between two energy channels are computed from light curves (e.g., Zhang 2002). The PSDs of light curves at essentially all wavelengths resemble power laws in frequency, $S(f) \propto f^{-b}$, with typically $b \sim 1$–3, usually steeper than PSDs found from Seyfert galaxies (Kataoka et al. 2001). Despite the popularity of PSDs for characterizing variability, their theoretical motivation has not been thoroughly explored (although see Mastichiadis et al. 2013).

In this paper, our goal is to bridge the gap between theory and observations by exploiting a powerful new mathematical approach for the modeling and interpretation of observed PSDs and time lags. Theoretically, the variability of blazars is often described by a continuity equation (e.g., Chiaberge & Ghisellini 1999; Li & Kusunose 2000; Böttcher & Chiang 2002; Chen et al. 2011, 2012). This equation describes the evolution of electrons in a compact region of the jet, which is homogeneous by assumption. The electrons are injected as a function of time and energy and the electron distribution evolves due to energy loss and escape. The expected electromagnetic emission observers might detect can be compared with observations (e.g., Böttcher & Reimer 2004; Joshi & Böttcher 2007). This can allow one to explore individual flares; however, in this paper, we take a different approach, by studying the electron continuity equation in the *Fourier domain*. This allows the exploration of individual flares, as well as the study of aggregated long-timescale variability of sources using Fourier transform-related quantities such as PSDs and phase and time lags. We focus here on long-timescale variability, including multiple epochs of flaring and quiescence. A similar study applying the same Fourier transform concept to the modeling of time lags in accreting Galactic black hole candidates has been recently carried out by Kroon & Becker (2014).

We begin in Section 2, by defining the Fourier transform and its inverse, and various other functions used throughout the rest

of the paper. In Section 3, we explore analytic solutions to the continuity equation in the Fourier domain, and present solutions in terms of PSDs. In Section 4, we explore the solutions in terms of time lags between different electron Lorentz factor "channels" as a function of Fourier frequency. We explore the expected synchrotron, SSC, and EC PSDs and Fourier frequency-dependent time lags in Section 5, including light travel time effects due to the emitting region's finite size. We discuss applications to some PSDs and time lags in the literature in Section 6, and conclude with a discussion of our simplifying assumptions and observational prospects in Section 7. Several of the detailed derivations are relegated to the appendices.

2. DEFINITIONS

Several definitions of the Fourier transform and associated quantities are used throughout the literature. Here we make the definitions used in this paper explicit. For a real function $x(t)$, we define the Fourier transform by

$$\tilde{x}(f) = \int_{-\infty}^{\infty} dt\; x(t)\, e^{2\pi i f t} = \int_{-\infty}^{\infty} dt\; x(t)\, e^{i\omega t}, \quad (1)$$

where $i^2 = -1$. We will indicate the Fourier transform by a tilde, the Fourier frequency by f, and the angular frequency by $\omega = 2\pi f$. We define the inverse Fourier transform by

$$x(t) = \int_{-\infty}^{\infty} df\; \tilde{x}(f)\, e^{-2\pi i f t} = \frac{1}{2\pi}\int_{-\infty}^{\infty} d\omega\; \tilde{x}(\omega)\, e^{-i\omega t}. \quad (2)$$

We define the PSD

$$S(f) = |\tilde{x}(f)|^2 = \tilde{x}(f)\tilde{x}^*(f), \quad (3)$$

where the asterisk indicates the complex conjugate. We will make use of the related representation of the Dirac δ-function

$$\delta(t - t_0) = \int_{-\infty}^{\infty} df\; e^{2\pi i f (t - t_0)}. \quad (4)$$

We will use two versions of the Heaviside function, a "step" function defined by

$$H(x) = \begin{cases} 1 & x > 0 \\ 0 & \text{otherwise} \end{cases}, \quad (5)$$

and the two-sided Heaviside "top-hat" function,

$$H(x; a, b) = \begin{cases} 1 & a < x < b \\ 0 & \text{otherwise} \end{cases}. \quad (6)$$

In Section 3.5 we will use the lower incomplete Gamma function given by

$$\gamma_g(a, x) = \int_0^x dy\; y^{a-1} e^{-y}. \quad (7)$$

3. CONTINUITY EQUATION IN FOURIER SPACE

3.1. General Solution

The evolution of electrons in a nonthermal plasma "blob" can be described by a continuity equation given by (e.g., Chiaberge & Ghisellini 1999; Li & Kusunose 2000; Böttcher & Chiang 2002; Chen et al. 2011, 2012)

$$\frac{\partial N_e}{\partial t} + \frac{\partial}{\partial \gamma}[\dot{\gamma}(\gamma, t) N_e(\gamma; t)] + \frac{N_e(\gamma; t)}{t_{\rm esc}(\gamma, t)} = Q(\gamma, t), \quad (8)$$

where $N_e(\gamma; t)\, d\gamma$ gives the number of electrons with Lorentz factor between γ and $\gamma + d\gamma$ at time t. Here $\dot{\gamma}(\gamma, t)$ is the rate at which electrons lose or gain energy, $t_{\rm esc}(\gamma, t)$ is the escape timescale, and $Q(\gamma, t)$ is the rate at which electrons are injected in the jet. In the simple model presented here, we will assume that the size of the plasma blob does not change with time, so that adiabatic losses can be neglected. We will also assume that the electron distribution in the blob is homogeneous and isotropic, and that variations occur throughout the blob simultaneously. This is a common and useful assumption, although it is somewhat unphysical, as in order for the blob to be causally connected, variations cannot propagate through the blob faster than the speed of light c.

Assuming that $\dot{\gamma}$ and $t_{\rm esc}$ are independent of t, we can take the Fourier transform of both sides of the continuity equation leading to

$$-2\pi i f \tilde{N}_e(\gamma, f) + \frac{\partial}{\partial \gamma}[\dot{\gamma}(\gamma)\tilde{N}_e(\gamma, f)] + \frac{\tilde{N}_e(\gamma, f)}{t_{\rm esc}(\gamma)} = \tilde{Q}(\gamma, f), \quad (9)$$

where $\tilde{Q}(\gamma, f)$ is the Fourier transformed source term. This is a linear ordinary first-order differential equation with a relatively simple solution. It is shown in Appendix A that if $\dot{\gamma} \leqslant 0$

$$\tilde{N}_e(\gamma, f) = \frac{1}{|\dot{\gamma}(\gamma)|}\int_{\gamma}^{\infty} d\gamma'\; \tilde{Q}(\gamma', f) \times \exp\left[-\int_{\gamma}^{\gamma'} \frac{d\gamma''}{|\dot{\gamma}(\gamma'')|}\left(\frac{1}{t_{\rm esc}(\gamma'')} - i\omega\right)\right]. \quad (10)$$

If $t_{\rm esc}$ is independent of γ and cooling is from synchro-Compton processes, so that $\dot{\gamma} = -\nu\gamma^2$, then one can perform the integral in the exponent, and

$$\gamma^2 \tilde{N}_e(\gamma, f) = \frac{1}{\nu}\exp\left[\frac{-1}{\nu\gamma}\left(\frac{1}{t_{\rm esc}} - i\omega\right)\right]\int_{\gamma}^{\infty} d\gamma'\; \tilde{Q}(\gamma', f) \times \exp\left[\frac{1}{\nu\gamma'}\left(\frac{1}{t_{\rm esc}} - i\omega\right)\right]. \quad (11)$$

3.2. Green's Function Solution

Consider an instantaneous injection of monoenergetic electrons with Lorentz factor γ_0 at $t = 0$. Then $\tilde{Q}(\gamma, f) = Q_0\delta(\gamma - \gamma_0)$ in Equation (11) and one gets

$$\gamma^2 \tilde{N}_e(\gamma, f) = \frac{Q_0}{\nu}\exp\left[\frac{-1}{\nu}\left(\frac{1}{\gamma} - \frac{1}{\gamma_0}\right)\left(\frac{1}{t_{\rm esc}} - i\omega\right)\right] \times H(\gamma_0 - \gamma). \quad (12)$$

The PSD is

$$S(\gamma, f) = |\gamma^2 \tilde{N}_e(\gamma, f)|^2 = \left[\frac{Q_0}{\nu}\right]^2 \exp\left[\frac{-2}{\nu t_{\rm esc}}\left(\frac{1}{\gamma} - \frac{1}{\gamma_0}\right)\right] \times H(\gamma_0 - \gamma). \quad (13)$$

The result is white noise for all electron Lorentz factors (γ) and Fourier frequencies (f).

3.3. Colored Noise

Since the PSDs of blazars resemble colored noise, and electrons are generally thought to be injected as power laws in γ, one might expect that

$$\tilde{Q}(\gamma, f) = Q_0 (f/f_0)^{-a/2} \gamma^{-q} H(\gamma; \gamma_1, \gamma_2) H(f; f_1, f_2), \quad (14)$$

where f_0 is some constant frequency and $a \geqslant 0$. That is, in the jet, shocks will occur randomly which accelerate and inject particles as a power-law distribution in γ between γ_1 and γ_2 with index q. We will deal only with frequencies in the range $f_1 \leqslant f \leqslant f_2$. These limits are needed for the PSD to be normalized to a finite value. Frequencies greater than the inverse of the blob's light crossing timescale are particularly unphysical, although we allow this for two reasons. First, it allows us to compare with other theoretical studies that allow variations faster than the light crossing timescale (e.g., Chiaberge & Ghisellini 1999; Zacharias & Schlickeiser 2013). Second, our blob is already unphysical, since we allow variations throughout the blob simultaneously in the blob's comoving frame. The normalization constant is related to the time-averaged power injected in electrons $\langle L_{\rm inj} \rangle$ over a time interval Δt by

$$Q_0 = \frac{2\pi \Delta t \langle L_{\rm inj} \rangle}{m_e c^2 G \sqrt{I_r^2 + I_i^2 - 2 I_r I_0 + I_0^2}}. \quad (15)$$

A derivation of this equation and definitions of the quantities G, I_r, I_i, and I_0 can be found in Appendix B. With $\tilde{Q}(\gamma, f)$, given by Equation (14), Equation (11) can be rewritten as

$$\gamma^2 \tilde{N}_e(\gamma, f) = Q_0 (f/f_0)^{-a/2} \exp\left[\frac{-1}{\nu\gamma}\left(\frac{1}{t_{\rm esc}} - i\omega\right)\right] \nu^{q-2} \times \left(\frac{1}{t_{\rm esc}} - i\omega\right)^{1-q} \int_{u_{\rm min}}^{u_{\rm max}} du\, u^{q-2}\, e^u, \quad (16)$$

where

$$u_{\rm min} = \frac{1}{\nu\gamma_2}\left(\frac{1}{t_{\rm esc}} - i\omega\right) \quad (17)$$

and

$$u_{\rm max} = \frac{1}{\nu \max(\gamma, \gamma_1)}\left(\frac{1}{t_{\rm esc}} - i\omega\right). \quad (18)$$

3.4. Electron Injection Index $q = 2$

It is instructive to look at the case where $q = 2$. In this case, the remaining integral in Equation (16) can easily be performed analytically. Then

$$\gamma^2 \tilde{N}_e(\gamma, f) = \frac{Q_0 (f/f_0)^{-a/2}}{1/t_{\rm esc} - i\omega} \exp\left[\frac{-1}{\nu\gamma}\left(\frac{1}{t_{\rm esc}} - i\omega\right)\right] \times [e^{u_{\rm max}} - e^{u_{\rm min}}], \quad (19)$$

and the PSD is

$$S(\gamma, f) = |\gamma^2 \tilde{N}_e(\gamma, f)|^2 = \exp\left[\frac{-2}{\nu\gamma t_{\rm esc}}\right] Q_0^2 (f/f_0)^{-a} \times \left(\frac{1}{t_{\rm esc}^2} + \omega^2\right)^{-1} \left\{ \exp\left[\frac{2}{\nu\gamma_2 t_{\rm esc}}\right] + \exp\left[\frac{2}{\nu \max(\gamma, \gamma_1) t_{\rm esc}}\right] - 2\exp\left[\frac{1}{\nu t_{\rm esc}}\left(\frac{1}{\max(\gamma, \gamma_1)} + \frac{1}{\gamma_2}\right)\right] \times \cos\left[\frac{\omega}{\nu}\left(\frac{1}{\max(\gamma, \gamma_1)} - \frac{1}{\gamma_2}\right)\right]\right\}. \quad (20)$$

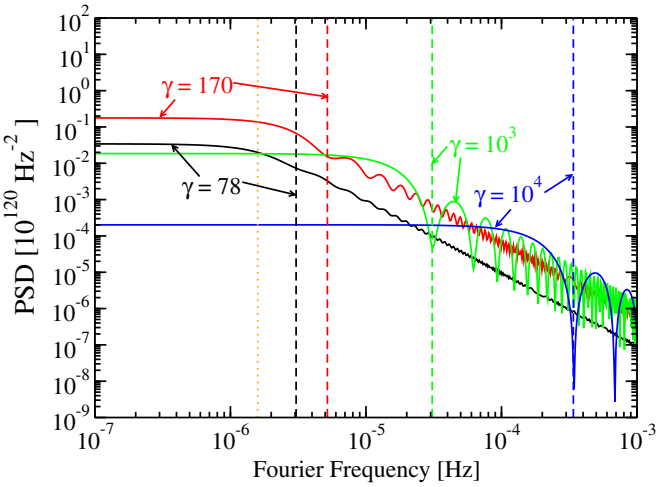

Figure 1. Electron PSD from Equation (20) resulting from an instantaneous flash ($a = 0$) of electrons injected with a power-law energy index $q = 2$. Here we set $t_{\rm esc} = 10^5$ s, $\nu = 3.1 \times 10^{-8}$ s^{-1}, $\langle L_{\rm inj} \rangle = 10^{42}$ erg s^{-1}, $\Delta t = 1$ yr, $\gamma_1 = 10^2$, $\gamma_2 = 10^5$. Dashed lines indicate $f = t_{\rm cool}^{-1}$ for each curve, and the dotted line indicates $f = (2\pi t_{\rm esc})^{-1}$.
(A color version of this figure is available in the online journal.)

We identify asymptotes for the PSD for $q = 2$, Equation (20). For these asymptotes we assume $\gamma \ll \gamma_2$.

1. If $1/(\nu t_{\rm esc}) \ll \gamma$ and $2\pi f/\nu \ll \gamma$, then

$$S(\gamma, f) \approx \frac{Q_0^2 (f/f_0)^{-a}}{\nu^2 \gamma^2}. \quad (21)$$

2. If $1/(\nu t_{\rm esc}) \ll \gamma \ll 2\pi f/\nu$, then

$$S(\gamma, f) \approx \frac{Q_0^2 (f/f_0)^{-a-2}}{f_0^2 \pi^2} \sin^2\left(\frac{\pi f}{\nu\gamma}\right). \quad (22)$$

3. If $\gamma \ll 1/(\nu t_{\rm esc})$, then

$$S(\gamma, f) \approx \frac{Q_0^2 (f/f_0)^{-a}}{1/t_{\rm esc}^2 + (2\pi f)^2} \exp\left[\frac{-2}{t_{\rm esc}}\left(\frac{1}{\nu\gamma} - t_{\rm cool}\right)\right] \times \left\{1 - \exp\left[-\frac{t_{\rm cool}}{t_{\rm esc}}\right] \cos[2\pi f t_{\rm cool}]\right\}, \quad (23)$$

where we define $t_{\rm cool}^{-1} = \nu \max(\gamma, \gamma_1)$.

The electron PSD resulting from Equation (20) is plotted in Figure 1 for parameters described in the caption, which are fairly standard ones for flat-spectrum radio quasars (FSRQs). We use $a = 0$ here, which represents an instantaneous injection of power-law particles at $t = 0$, to more easily display the observable features, a number of which are present. For the $\gamma = 78$, 170, and 10^3 curves, where $\gamma \ll (\nu t_{\rm esc})^{-1}$), a break in the power law from

$$S(\gamma, f) \propto f^{-a}$$

to

$$S(\gamma, f) \propto f^{-(a+2)}$$

is apparent, and the break frequency is at

$$f \approx (2\pi t_{\rm esc})^{-1}.$$

This is in agreement with asymptote 3 above. In general, by examining asymptote 3, it is clear that for low γ a break in the PSD will be found at a frequency of $f = (2\pi t_{\rm esc})^{-1}$. Since the PSD measures periodic variability, this indicates that for low γ, periodic variability on timescales less than the escape timescale is less preferred. This is because electrons will always be escaping at a single timescale, which does not vary with time. One can also see in the $\gamma = 170$ curve in Figure 1 at high f structure related to the cosine seen in asymptote 3, with local minima at integer multiples of $t_{\rm cool}$.

In the $\gamma = 10^3$ and $\gamma = 10^4$ curves, at high γ ($\gamma \gg (\nu t_{\rm esc})^{-1}$) the PSD will transition from

$$S(\gamma, f) \propto f^{-a}$$

to

$$S(\gamma, f) \propto f^{-(a+2)},$$

but in this case the transition is at

$$f = t_{\rm cool}^{-1},$$

in agreement with asymptotes 1 and 2. Thus, variability on timescales less than the cooling timescales will be less periodic, since cooling on those smaller timescales will always be present. It is also clear that at high f minima from the $\sin^2$ term in asymptote 2 occur at integer multiples of $t_{\rm cool}^{-1}$. Since at high values of γ, where the cooling is strongest, cooling on timescales $t_{\rm cool}$ will be immediate, and so periodic variability on timescales that are integer multiples of $t_{\rm cool}$ will also be strongly avoided.

3.5. Electron Injection Index $q \neq 2$

In this case, there is no simple analytic solution to Equation (16), although it can be written with the incomplete Gamma function as

$$\gamma^2 \tilde{N}_e(\gamma, f) = Q_0 (f/f_0)^{-a/2} \exp\left[\frac{-1}{\nu\gamma}\left(\frac{1}{t_{\rm esc}} - i\omega\right)\right] \nu^{q-2} \times \left(i\omega - \frac{1}{t_{\rm esc}}\right)^{1-q} [\gamma_g(q-1, -u_{\rm max}) - \gamma_g(q-1, -u_{\rm min})]. \quad (24)$$

We compute the function numerically, and results can be seen in Figure 2 for $q = 2.5$. This confirms the features seen in the $q = 2$ case are also seen for other values of q, although the minima at high γ are not as pronounced.

4. TIME LAGS

The phase lag between two electron Lorentz factor "channels," γ_a and γ_b, as a function of Fourier frequency (f) can be calculated from

$$\Delta\phi(\gamma_a, \gamma_b, f) = \arctan\left\{\frac{Y_I(\gamma_a, \gamma_b, f)}{Y_R(\gamma_a, \gamma_b, f)}\right\}, \quad (25)$$

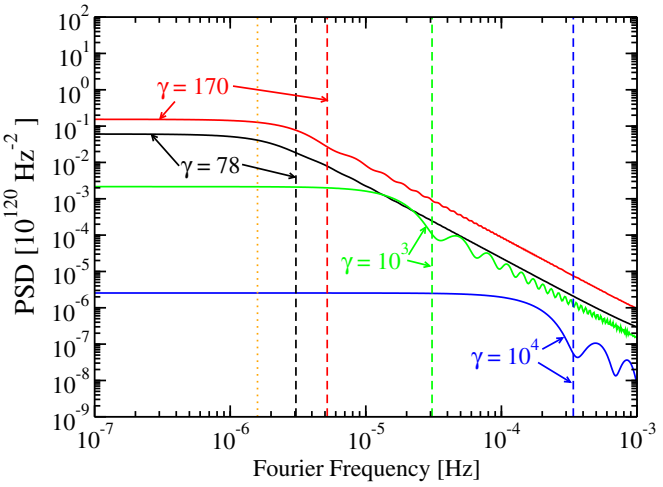

Figure 2. Same as Figure 1, except that we set the injection power-law index $q = 2.5$.

(A color version of this figure is available in the online journal.)

where

$$[\gamma_a^2 \tilde{N}_e(\gamma_a, f)][\gamma_b^2 \tilde{N}_e(\gamma_b, f)]^* = Y_R(\gamma_a, \gamma_b, f) + i Y_I(\gamma_a, \gamma_b, f). \quad (26)$$

This implies that

$$Y_R(\gamma_a, \gamma_b, f) = {\rm Re}\left[\gamma_a^2 \tilde{N}_e(\gamma_a, f)\right]{\rm Re}\left[\gamma_b^2 \tilde{N}_e(\gamma_b, f)\right] + {\rm Im}\left[\gamma_a^2 \tilde{N}_e(\gamma_a, f)\right]{\rm Im}\left[\gamma_b^2 \tilde{N}_e(\gamma_b, f)\right] \quad (27)$$

and

$$Y_I(\gamma_a, \gamma_b, f) = {\rm Re}\left[\gamma_b^2 \tilde{N}_e(\gamma_b, f)\right]{\rm Im}\left[\gamma_a^2 \tilde{N}_e(\gamma_a, f)\right] - {\rm Re}\left[\gamma_a^2 \tilde{N}_e(\gamma_a, f)\right]{\rm Im}\left[\gamma_b^2 \tilde{N}_e(\gamma_b, f)\right]. \quad (28)$$

The time lag can be calculated from the phase lag,

$$\Delta T(\gamma_a, \gamma_b, f) = \frac{\Delta\phi(\gamma_a, \gamma_b, f)}{2\pi f}. \quad (29)$$

For our solution, Equation (19), the time lag is

$$\Delta T(\gamma_a, \gamma_b, f) = \frac{1}{2\pi f} \arctan\left\{\frac{Z_I(\gamma_a, \gamma_b, f)}{Z_R(\gamma_a, \gamma_b, f)}\right\}, \quad (30)$$

where

$$Z_I(\gamma_a, \gamma_b, f) = \exp\left[-\frac{1}{\nu t_{\rm esc}}\left(\frac{1}{\gamma_a} + \frac{1}{\gamma_b}\right)\right] \times \left\{\exp\left[\frac{2}{\nu t_{\rm esc}\gamma_2}\right]\sin\left[\frac{\omega}{\nu}\left(\frac{1}{\gamma_a} - \frac{1}{\gamma_b}\right)\right] + \exp\left[\frac{1}{\nu t_{\rm esc}}\left(\frac{1}{\max(\gamma_1, \gamma_a)} + \frac{1}{\max(\gamma_1, \gamma_b)}\right)\right] \times \sin\left[\frac{\omega}{\nu}\left(\frac{1}{\max(\gamma_1, \gamma_b)} - \frac{1}{\gamma_b} + \frac{1}{\gamma_a} - \frac{1}{\max(\gamma_1, \gamma_b)}\right)\right] - \exp\left[\frac{1}{\nu t_{\rm esc}}\left(\frac{1}{\max(\gamma_1, \gamma_a)} + \frac{1}{\gamma_2}\right)\right] \times \sin\left[\frac{\omega}{\nu}\left(\frac{1}{\gamma_a} - \frac{1}{\max(\gamma_1, \gamma_a)} + \frac{1}{\gamma_2} - \frac{1}{\gamma_b}\right)\right]$$

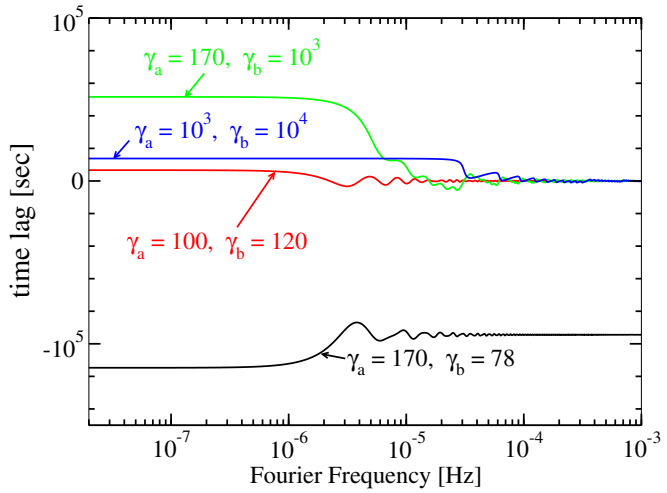

Figure 3. Electron time lags with various values of γ_a and γ_b. Parameters are the same as in Figure 1.

(A color version of this figure is available in the online journal.)

$$- \exp\left[\frac{1}{\nu t_{\rm esc}}\left(\frac{1}{\gamma_2} + \frac{1}{\max(\gamma_1, \gamma_b)}\right)\right] \times \sin\left[\frac{\omega}{\nu}\left(\frac{1}{\gamma_a} - \frac{1}{\gamma_2} + \frac{1}{\max(\gamma_1, \gamma_b)} - \frac{1}{\gamma_b}\right)\right]\Bigg\} \quad (31)$$

and $Z_R(\gamma_a, \gamma_b, f)$ is the same as $Z_I(\gamma_a, \gamma_b, f)$ except with cos in place of sin. Several examples of electron time lags can be seen in Figure 3.

For $f \ll \nu\gamma_a/(2\pi)$ and $f \ll \nu\gamma_b/(2\pi)$ the time delay will be approximately independent of frequency, with value

$$\Delta T(\gamma_a, \gamma_b, f) \approx \frac{1}{\nu}\frac{A_I(\gamma_a, \gamma_b)}{A_R(\gamma_a, \gamma_b)}, \quad (32)$$

where

$$A_I(\gamma_a, \gamma_b, f) = \left(\frac{1}{\gamma_a} - \frac{1}{\gamma_b}\right)\exp\left[\frac{-1}{\nu t_{\rm esc}}\left(\frac{1}{\gamma_a} + \frac{1}{\gamma_b}\right)\right] + \frac{1}{\gamma_b}\exp\left[\frac{-1}{\nu t_{\rm esc}\gamma_b}\right] - \frac{1}{\gamma_a}\exp\left[\frac{-1}{\nu t_{\rm esc}\gamma_a}\right] \quad (33)$$

and

$$A_R(\gamma_a, \gamma_b, f) = 1 + \exp\left[\frac{-1}{\nu t_{\rm esc}}\left(\frac{1}{\gamma_a} + \frac{1}{\gamma_b}\right)\right] - \exp\left[\frac{-1}{\nu t_{\rm esc}\gamma_b}\right] - \exp\left[\frac{-1}{\nu t_{\rm esc}\gamma_a}\right], \quad (34)$$

where we also assumed $\gamma_1 < \gamma_a \ll \gamma_2$ and $\gamma_1 < \gamma_b \ll \gamma_2$. At these low values of f, the lags are positive for $\gamma_a > \gamma_b$ indicating the smaller γ lags behind the larger γ. This is due to the fact that electrons with smaller γ will take longer to cool than those with larger γ. If also $(\nu t_{\rm esc})^{-1} \ll \gamma_a$ and $(\nu t_{\rm esc})^{-1} \ll \gamma_b$ then

$$\Delta T(\gamma_a, \gamma_b, f) \approx \frac{1}{2\nu}\left(\frac{1}{\gamma_a} - \frac{1}{\gamma_b}\right). \quad (35)$$

An example of this can be seen in Figure 3, with the $\gamma_a = 10^3$, $\gamma_b = 10^4$ curve. If $\gamma_a \ll (\nu t_{\rm esc})^{-1} \ll \gamma_b$ then

$$\Delta T(\gamma_a, \gamma_b, f) \approx t_{\rm esc}\left\{1 - \frac{1}{\nu t_{\rm esc}\gamma_b} - \frac{1}{\nu t_{\rm esc}\gamma_a}\exp\left[\frac{-1}{\nu t_{\rm esc}\gamma_a}\right]\right\}. \quad (36)$$

In Figure 3, an example can be seen with the $\gamma_a = 170$, $\gamma_b = 10^3$ curve.

If $\gamma_a \ll (\nu t_{\rm esc})^{-1}$ and $\gamma_b \ll (\nu t_{\rm esc})^{-1}$ then $\Delta T(\gamma_a, \gamma_b, f) \to 0$. In Figure 3, the curve that most closely approximates this is the $\gamma_a = 100$, $\gamma_b = 120$ curve.

At high f, The behavior is quite complex. By inspecting Equation (31), we can see that the important frequencies are those that make the sine or cosine terms go to 0. They will be the integer or half-integer multiples of

$$f = t_{{\rm cool},a}^{-1} = \nu\gamma_a \quad (37)$$

$$f = t_{{\rm cool},b}^{-1} = \nu\gamma_b \quad (38)$$

$$f = (t_{{\rm cool},a} - t_{{\rm cool},b})^{-1}. \quad (39)$$

There are many local minima and maxima at the integer or half-integer multiples of these values.

5. EMISSION AND LIGHT TRAVEL TIME EFFECTS

In the previous sections we have explored the PSD and time lags for the electron distribution. However, what is observed is the emission of these electrons, through synchrotron or Compton scattering. We will assume that the emitting region is spherical with co-moving radius R' and homogeneous, containing a tangled magnetic field of strength B. The blob is moving with a relativistic speed βc (c being the speed of light), giving it a bulk Lorentz factor $\Gamma = (1 - \beta^2)^{-1/2}$. The blob is moving with an angle θ to the line of sight giving it a Doppler factor $\delta_D = [\Gamma(1 - \beta\cos(\theta))]^{-1}$. Although we make the simplifying assumption that the blob is homogeneous, with variations in the electron distribution taking place throughout the blob simultaneously, since it has a finite size, photons will reach the observer earlier from the closer part than the farther part, and thus one must integrate over the time in the past, t'. This is similar to the "time slices" of Chiaberge & Ghisellini (1999). We note again that Fourier frequencies higher than the inverse of the light crossing timescale are unphysical in the simple model we present here.

5.1. Synchrotron and External Compton

Taking the light travel time into account, in the δ-approximation the observed νF_ν flux at observed energy ϵ (in units of the electron rest energy) from synchrotron or Compton scattering of an external isotropic monochromatic radiation field as a function of the observer's time t is

$$F_\epsilon(t) = \frac{K(1+z)}{t_{\rm lc}\delta_{\rm D}}\int_0^{2R'/c} dt'\, N_e\left(\gamma'; \frac{t\delta_D}{1+z} - t'\right), \quad (40)$$

where

$$t_{\rm lc} = \frac{2R'(1+z)}{c\delta_{\rm D}} \quad (41)$$

is the light crossing time in the observer's frame. A derivation of the light travel time effect can be found in Appendix C. For synchrotron emission,

$$K = K_{\rm sy} = \frac{\delta_D^4}{6\pi d_L^2} c\sigma_{\rm T} u_B \gamma_{\rm sy}'^3, \quad (42)$$

and

$$\gamma' = \gamma'_{\rm sy} = \sqrt{\frac{\epsilon(1+z)}{\delta_D \epsilon_B}}. \quad (43)$$

The Thomson cross-section is $\sigma_{\rm T} = 6.65 \times 10^{-25}$ cm^2, the Poynting flux energy density is $u_B = B^2/(8\pi)$, $\epsilon_B = B/B_c$ where $B_c = 4.414 \times 10^{13}$ G, the redshift of the source is z, and the luminosity distance to the source is d_L. For EC scattering,

$$K = K_{\rm EC} = \frac{\delta_D^6}{6\pi d_L^2} c\sigma_{\rm T} u_0 \gamma'^3_{\rm EC}, \quad (44)$$

$$\gamma' = \gamma'_{\rm EC} = \frac{1}{\delta_D}\sqrt{\frac{\epsilon(1+z)}{2\epsilon_0}} \quad (45)$$

(Dermer & Menon 2009). Here the external radiation field energy density and photon energy (in units of the electron rest energy) are u_0 and ϵ_0, respectively. This approximation is valid in the Thomson regime, i.e., when $\gamma' \lesssim (\Gamma\epsilon_0)^{-1}$. Primed quantities refer to the frame co-moving with the emitting region. The cooling rate parameter is

$$\nu = \frac{4}{3m_e c^2} c\sigma_{\rm T}(u_B + \Gamma^2 u_0), \quad (46)$$

where we ignore the effects of SSC cooling.

It is shown in Appendix D that the Fourier transform of Equation (40) is

$$\tilde{F}_\epsilon(f) = \frac{K(1+z)}{2\pi i f t_{\rm lc}\delta_{\rm D}} \tilde{N}_e\left(\gamma', \frac{(1+z)f}{\delta_{\rm D}}\right) \times \left\{\exp\left[\frac{4\pi i f (1+z) R'}{c\delta_{\rm D}}\right] - 1\right\}. \quad (47)$$

Equation (47) implies the PSD of the synchrotron or EC flux is

$$S(\epsilon, f) = |\tilde{F}_\epsilon(f)|^2 = \frac{K^2(1+z)^2}{(\pi f t_{\rm lc}\delta_{\rm D})^2} \times \left|\tilde{N}_e\left(\gamma', \frac{(1+z)f}{\delta_{\rm D}}\right)\right|^2 \sin^2(\pi f t_{\rm lc}). \quad (48)$$

If the emitting region is very compact, i.e., if $R' \ll c\delta_{\rm D}(2f(1+z))^{-1}$, then

$$S(\epsilon, f) \approx \frac{K^2(1+z)^2}{(\pi f t_{\rm lc}\delta_{\rm D})^2} \left|\tilde{N}_e\left(\gamma', \frac{(1+z)f}{\delta_{\rm D}}\right)\right|^2 (\pi f t_{\rm lc})^2$$
$$S(\epsilon, f) \approx \frac{K^2(1+z)^2}{\delta_{\rm D}^2} \left|\tilde{N}_e\left(\gamma', \frac{(1+z)f}{\delta_{\rm D}}\right)\right|^2. \quad (49)$$

So in the case of a very compact emitting region, the light travel time effects play no part in the PSD, as one would expect.

The observed flux PSDs from synchrotron and EC one would expect are shown in Figure 4, calculated from Equations (48) and (20). The parameter values are the same as in Figure 1, with additional parameters given in the caption. The seed photon source is assumed to be Lyα photons, presumably from a broad-line region. Again, parameters are chosen to be consistent with

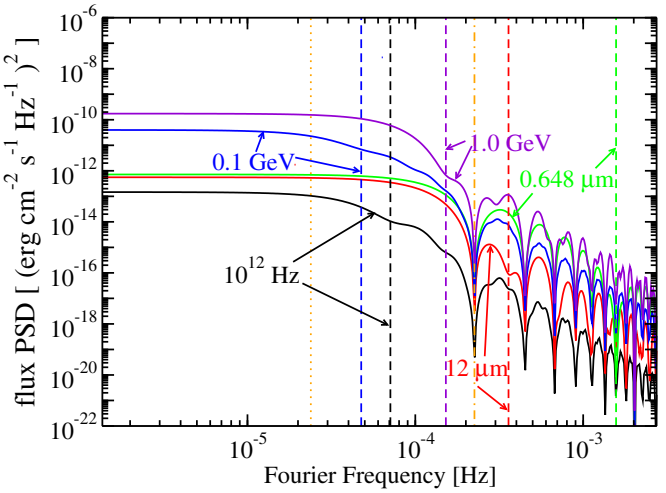

Figure 4. Flux PSD computed from Equations (48) and (20) using the same parameters as in Figure 1. Additional parameters are $\delta_D = \Gamma = 30$, $B = 1$ G, $u_0 = 10^{-3}$ erg cm^{-3}, $\epsilon_0 = 2 \times 10^{-5}$, $R' = 10^{15}$ cm, and $z = 1$. At this redshift with a cosmology $(h, \Omega_m, \Omega_\Lambda) = (0.7, 0.3, 0.7)$, $d_L = 2 \times 10^{28}$ cm. The observed photon frequency, wavelength, or energy is shown, along with $t_{\rm cool}^{-1}$ for each curve (dashed lines), $(2\pi t_{\rm esc})^{-1}$ (dotted line), and $t_{\rm lc}^{-1}$ (dashed-dotted line), all computed in the observer's frame.

(A color version of this figure is available in the online journal.)

those one would expect from an FSRQ. Synchrotron PSDs are shown for 10^{12} Hz, 12 μm (the *WISE* W3 filter's central wavelength), and 0.648 μm (the central wavelength of the Johnson *R* band). EC PSDs are shown for 0.1 and 1.0 GeV, which are within the *Fermi*-LAT energy range. Frequencies lower than 10^{12} Hz can be affected by synchrotron self-absorption, which is not considered in this paper. X-rays are not shown as they are likely dominated by SSC emission, which is considered in Section 5.2 below. Also note that in real FSRQs the 12 μm PSD could suffer from contamination from dust torus emission (e.g., Malmrose et al. 2011) and the *R* band could suffer from contamination from accretion disk emission, and we do not take either of these possibilities into account.

Figure 4 shows many of the features seen in Figure 1. For photons generated from electrons with low γ' the PSDs show a break from

$$S(\epsilon, f) \propto f^{-a}$$

to

$$S(\epsilon, f) \propto f^{-(a+2)}$$

at approximately

$$f = (2\pi t_{\rm esc})^{-1},$$

as seen in the 10^{12} Hz and 0.1 GeV PSDs. For synchrotron, if $u_B \ll \Gamma^2 u_0$, as is usually the case for FSRQs, this regime occurs when

$$\nu \ll \nu_{\rm cr,sy} = 10^{13}\ {\rm Hz} \left(\frac{\delta_D}{\Gamma}\right)\left(\frac{\Gamma}{30}\right)^{-3}\left(\frac{u_0}{10^{-3}\ {\rm erg\ cm^{-3}}}\right)^{-2} \times \left(\frac{t_{\rm esc}}{10^5\ {\rm s}}\right)^{-2}\left(\frac{B}{1\ {\rm G}}\right)\frac{1}{1+z}. \quad (50)$$

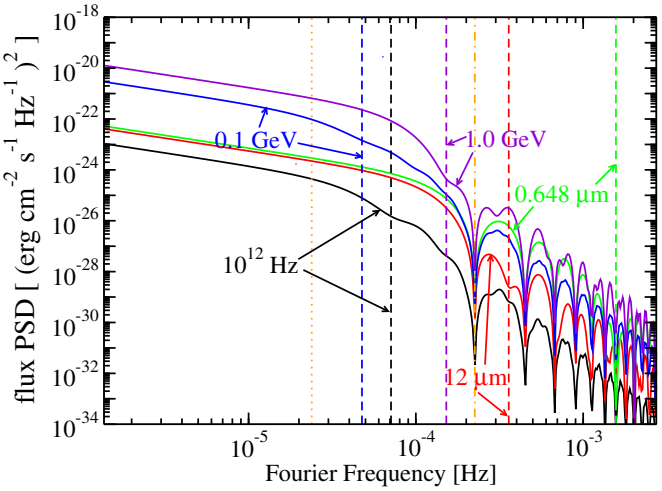

Figure 5. Same as Figure 4 except that we set $a = 1$.
(A color version of this figure is available in the online journal.)

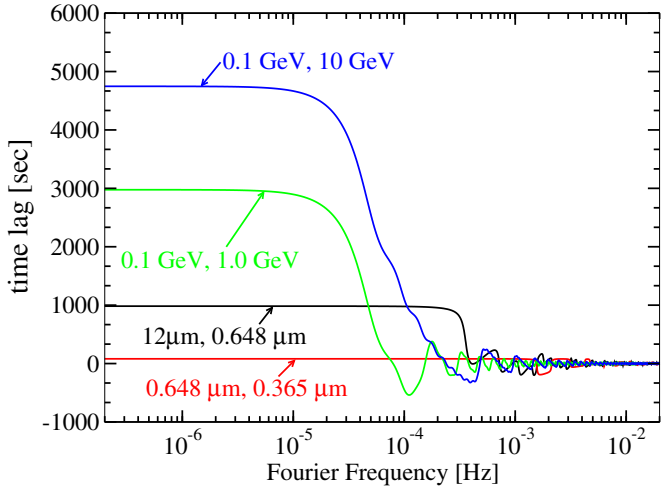

Figure 6. Observed time lags as a function of observed Fourier frequency. Parameters are the same as in Figure 1, with parameters the same as Figures 1 and 4. The 0.648 μm (central wavelength of R band) and 0.365 μm (central wavelength of U band) are from synchrotron, while the 0.1, 1.0, and 10 GeV emission is from EC.
(A color version of this figure is available in the online journal.)

For EC, this regime occurs when

$$m_e c^2 \epsilon \ll E_{\rm cr,EC} = 2\ {\rm GeV} \left(\frac{\delta_D}{\Gamma}\right)^2 \left(\frac{\Gamma}{30}\right)^{-2} \times \left(\frac{u_0}{10^{-3}\ {\rm erg\ cm^{-3}}}\right)^{-2} \left(\frac{t_{\rm esc}}{10^5}\right)^{-2} \left(\frac{\epsilon_0}{2\times 10^{-5}}\right) \frac{1}{1+z}. \quad (51)$$

If $u_B \gg \Gamma^2 u_0$, then

$$\nu_{\rm cr,sy} = 5\times 10^{15}\ {\rm Hz} \left(\frac{\delta_D}{30}\right)^2 \left(\frac{t_{\rm esc}}{10^5\ {\rm s}}\right)^{-2} \left(\frac{B}{1\ {\rm G}}\right)^{-3} \frac{1}{1+z} \quad (52)$$

and

$$E_{\rm cr,EC} = 1\ {\rm TeV} \left(\frac{\delta_D}{30}\right)^2 \left(\frac{t_{\rm esc}}{10^5}\right)^{-2} \left(\frac{B}{1\ {\rm G}}\right)^{-4} \times \left(\frac{\epsilon_0}{2\times 10^{-5}}\right) \frac{1}{1+z}. \quad (53)$$

For photons generated from electrons with high γ' ($\nu \gg \nu_{\rm cr,sy}$ or $m_e c^2 \epsilon \gg E_{\rm cr,EC}$ for synchrotron or EC, respectively), minima are seen at integer multiples of $f = t_{\rm cool}^{-1}$, as seen in the 12 μm, R band and 1.0 GeV PSDs, as well as a break of 2 at approximately $f = t_{\rm cool}^{-1}$. There is an additional feature in Figure 4 not seen in Figure 1 related to the light travel timescale. In agreement with Equation (48), $\sin^2$ minima can be seen at integer multiples of $f = 1/t_{\rm lc}$ which appear in the PSDs at all photon energies. Additionally, there is a break of 2 at approximately this frequency, in agreement with Equations (48) and (49).

In Figure 5 we plot observed PSDs for the parameter $a = 1$. This demonstrates that our model can reproduce any color noise in a synchrotron or EC PSD for an appropriate choice of a, and that the features described above are preserved for different values of a.

For synchrotron or EC emission, in our simple model, the time delays will play no role in the Fourier frequency-dependent time lags (Section 4). It is easy enough to see by inspecting Equation (47) that terms associated with the light travel time will cancel when calculating time lags. However, one must be careful to shift the time lag and frequency into the observed frame by multiplying by $(1+z)/\delta_{\rm D}$ and $\delta_{\rm D}/(1+z)$, respectively. An example of observed time lags can be seen in Figure 6 for synchrotron emission and EC emission.

5.2. Synchrotron Self-Compton

The synchrotron-producing electrons will also Compton scatter the synchrotron radiation they produce, leading to SSC emission. Again, assuming the blob is homogeneous, and taking into account light travel time effects, we have

$$F_\epsilon^{\rm SSC}(t) = \frac{K_{\rm SSC}(1+z)}{t_{\rm lc}\delta_D} \int_0^{2R'/c} dt' \int_0^{\min[\epsilon', \epsilon'^{-1}]} \frac{d\epsilon_i'}{\epsilon_i'} \times N_e\left(\sqrt{\frac{\epsilon'}{\epsilon_i'}}; \frac{t\delta_{\rm D}}{1+z} - t'\right) N_e\left(\sqrt{\frac{\epsilon_i'}{\epsilon_B}}; \frac{t\delta_{\rm D}}{1+z} - t'\right), \quad (54)$$

where

$$K_{\rm SSC} = \frac{\delta_D^4 c \sigma_{\rm T}^2 R' u_B}{12\pi d_L^2 V'} \left(\frac{\epsilon}{\epsilon_B}\right)^{3/2}, \quad (55)$$

$$V' = \frac{4}{3}\pi R'^3 \quad (56)$$

is the blob volume in the comoving frame, and

$$\epsilon' = \frac{(1+z)\epsilon}{\delta_D} \quad (57)$$

(Dermer & Menon 2009). Following the same procedure for synchrotron and EC, for the Fourier transform we get

$$\tilde{F}_\epsilon^{\rm SSC}(f) = \frac{K_{\rm SSC}(1+z)}{2\pi i t_{\rm lc} f \delta_{\rm D}} \left\{\exp\left[\frac{4\pi i f (1+z) R'}{c\delta_{\rm D}}\right] - 1\right\} \int_{-\infty}^{\infty} df' \times \int_0^{\min[\epsilon', \epsilon'^{-1}]} \frac{d\epsilon_i'}{\epsilon_i'} \tilde{N}_e\left(\sqrt{\frac{\epsilon'}{\epsilon_i'}}; \frac{(1+z)f}{\delta_{\rm D}} - f'\right) \tilde{N}_e\left(\sqrt{\frac{\epsilon_i'}{\epsilon_B}}; f'\right). \quad (58)$$

Note, however, that we ignore the effects of SSC cooling. In this case, $\dot{\gamma}(\gamma)$ would be dependent on the electron distribution, $\gamma^2 N(\gamma; t)$ (or $\gamma^2 \tilde{N}(\gamma, f)$) leading to a non-linear differential equation. This is treated in detail for the continuity equation by Schlickeiser (2009), Schlickeiser et al. (2010), and Zacharias & Schlickeiser (2010, 2012a, 2012b). The SSC PSD is

$$S^{\rm SSC}(\epsilon, f) = \left|\tilde{F}_\epsilon^{\rm SSC}(f)\right|^2 = \left(\frac{K_{\rm SSC}(1+z)}{2\pi t_{\rm lc} f \delta_{\rm D}}\right)^2 \times \sin^2(\pi f t_{\rm lc}) |I(\epsilon, f)|^2, \quad (59)$$

where

$$I(\epsilon, f) = \int_{-\infty}^{\infty} df' \int_0^{\min[\epsilon', \epsilon'^{-1}]} \frac{d\epsilon_i'}{\epsilon_i'} \tilde{N}_e\left(\sqrt{\frac{\epsilon'}{\epsilon_i'}}; \frac{(1+z)f}{\delta_{\rm D}} - f'\right) \times \tilde{N}_e\left(\sqrt{\frac{\epsilon_i'}{\epsilon_B}}; f'\right). \quad (60)$$

At low frequencies, $f \ll (\pi t_{\rm lc})^{-1}$ and $f' \ll (\pi t'_{\rm esc})^{-1}$,

$$S^{\rm SSC}(\epsilon, f) \approx \frac{K_{\rm SSC}^2 (1+z)^2}{4\delta_{\rm D}^2} (Q_0 t_{\rm esc})^4 \left(\frac{\delta_{\rm D}\epsilon_B}{\epsilon(1+z)}\right)^2 \times [C_1(a, \epsilon_{\rm min}, \epsilon_{\rm max}) C_2(a, f_{\rm min}, f_{\rm max})]^2, \quad (61)$$

where

$$C_1(a, \epsilon_{\rm min}, \epsilon_{\rm max}) = \int_{\epsilon_{\rm min}}^{\epsilon_{\rm max}} \frac{d\epsilon_i'}{\epsilon_i'} \left\{ \exp\left[\frac{-1}{\nu t_{\rm esc}}\left(\sqrt{\frac{\epsilon_i'}{\epsilon'}} + \sqrt{\frac{\epsilon_b}{\epsilon_i'}}\right)\right] - \exp\left[\frac{-1}{\nu t_{\rm esc}}\sqrt{\frac{\epsilon_i'}{\epsilon'}}\right] - \exp\left[\frac{-1}{\nu t_{\rm esc}}\sqrt{\frac{\epsilon_b}{\epsilon_i}}\right] + 1 \right\}, \quad (62)$$

$$C_2(a, f_{\rm min}, f_{\rm max}) = f_0^a \times \begin{cases} (f_{\rm max}^{1-a} - f_{\rm min}^{1-a})(1-a)^{-1} & a \neq 1 \\ \ln(f_{\rm max}/f_{\rm min}) & a = 1 \end{cases}, \quad (63)$$

$$f_{\rm min} = \max\left[f_1, \frac{(1+z)f}{\delta_{\rm D}} - f_2\right], \quad (64)$$

$$f_{\rm max} = \min\left[f_2, \frac{(1+z)f}{\delta_{\rm D}} - f_1\right], \quad (65)$$

$$\epsilon_{\rm min} = \max\left[\gamma_1^2 \epsilon_B, \epsilon'/\gamma_2\right], \quad (66)$$

and

$$\epsilon_{\rm max} = \min\left[\epsilon', \epsilon'^{-1}, \gamma_2^2 \epsilon_B, \epsilon'/\gamma_1^2\right]. \quad (67)$$

If $f_2 > (1+z)f/\delta_{\rm D} \gg f_1$, then at low frequencies the SSC PSD will go as

$$S^{\rm SSC}(\epsilon, f) \propto f^{-(2a-2)}.$$

Synchrotron and SSC PSDs are shown in Figure 7. The parameters were chosen to be those one would expect from a high-peaked BL Lac object. At low frequency, they agree with the asymptote above. Here, the PSDs are flatter (the PSD power-law index is smaller) than for synchrotron or EC. At high frequency the behavior is complex, but the features from the light crossing timescale are apparent. There are no features associated with the cooling timescale of the electrons which produce SSC photons, since the SSC emission for a particular observed energy will be produced by a broad range of electrons. This is in contrast to synchrotron or EC where the photons at a particular energy can be approximated as being produced by a single electron Lorentz factor.

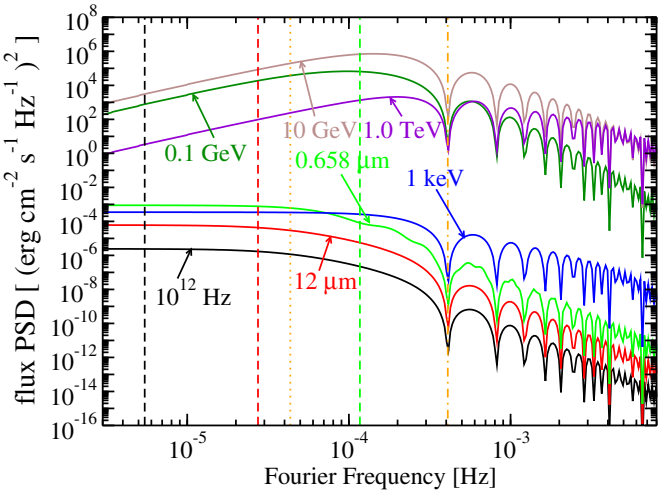

Figure 7. Synchrotron and SSC flux PSD computed from Equation (59). Parameters are the same as in Figure 4, except $u_0 = 0$ and $z = 0.1$, giving $d_L = 1.4 \times 10^{27}$ cm with a cosmology where $(h, \Omega_m, \Omega_\Lambda) = (0.7, 0.3, 0.7)$. For the synchrotron curves, the frequency associated with $t_{\rm cool}$ for the electrons that produce those photons is shown as the dashed lines. The dotted curve indicates the frequency $(2\pi t_{\rm esc})^{-1}$ and the dashed-dotted line indicates the frequency $t_{\rm lc}^{-1}$, all computed in the observer's frame.

(A color version of this figure is available in the online journal.)

6. APPLICATIONS

The PSDs of blazars are almost always power laws, $S(\epsilon, f) \propto f^{-b}$ (i.e., colored noise), although there is sometimes evidence that they deviate from this. As seen in Section 5, our model can reproduce this, since in our model at low frequency for synchrotron or EC the PSD goes as $S^{\rm sy/EC}(\epsilon, f) \propto f^{-a}$ and for SSC $S^{\rm SSC}(\epsilon, f) \propto f^{-(2a-2)}$, where a is the parameter from Equation (14). For an appropriate choice of a, it can reproduce any power-law PSD. At higher frequencies, our model predicts features in PSDs that deviate from a strict single power law. In this section, we explore some of the applications of our model to observed PSDs from the literature.

6.1. The VHE Gamma-Ray PSD of PKS 2155−304

In the PSD measured by HESS from PKS 2155−304, Aharonian et al. (2007) found a power law with $S(\epsilon, f) \propto f^{-2}$, out to $f \gtrsim 10^{-3}$ Hz. There does appear to be a minimum feature at $f \approx 1.2 \times 10^{-3}$ Hz. It is not clear if there is a break in the PSD at higher frequencies that this. If this feature is associated with the light crossing timescale, then

$$R' \approx \frac{c t_{\rm lc} \delta_{\rm D}}{2(1+z)} = 6.5 \times 10^{14} \left(\frac{\delta_{\rm D}}{60}\right) \text{ cm}. \quad (68)$$

Such a high Doppler factor is needed for these flares to avoid $\gamma\gamma$ attenuation (Begelman et al. 2008; Finke et al. 2008). Since the γ-rays from this source are likely associated with the SSC mechanism for this source, this association in unambiguous.

There are no PSD features associated with a cooling timescale for SSC, as shown in Section 5.2.

6.2. The X-Ray Timing Properties of Mrk 421

Zhang (2002) constructed PSDs from *BeppoSAX* data on Mrk 421. They construct PSDs with data from two energy intervals: 0.1–2 keV, and 2–10 keV (see their Figure 4). Both PSDs show a minimum feature at $f \approx 4.3 \times 10^{-5}$ Hz. Although the feature is tentative, since it is only dependent on one point for each PSD, and there are no error bars, the fact that the feature is at the same frequency in both energy bands is a hint that the feature is associated with the light crossing timescale. In this case, $t_{\rm lc} = 2.3 \times 10^4$ s $= 6.4$ hr and

$$R' \approx \frac{ct_{\rm lc}\delta_{\rm D}}{2(1+z)} = 1.0 \times 10^{16}\left(\frac{\delta_{\rm D}}{30}\right) \text{ cm}. \quad (69)$$

Zhang (2002) also provides time lags as a function of Fourier frequency between the two energy bands, 0.1–2 keV and 2–10 keV (see their Figure 5), giving us an opportunity to compare them with the results of Section 4. Zhang (2002) finds time lags at $f \lesssim 10^{-4}$ Hz that are approximately constant at $\Delta T \approx 10^3$ s. The approximate independence of the lag with frequency implies that the lag is in the regime where $(\nu t_{\rm esc})^{-1} \ll \gamma_a$ and $(\nu t_{\rm esc})^{-1} \ll \gamma_b$, and the lag $\Delta T'$ can be approximated by Equation (35). Note that this equation gives the lag in the jet comoving frame; in the observer's frame, $\Delta T = \Delta T'(1+z)/\delta_D$. The X-rays for Mrk 421 are likely produced by synchrotron emission and the external energy density (u_0) is likely to be negligible for a BL Lac object, so one can combine Equation (35) with Equations (43) and (46) to get

$$B = \frac{B_c}{(\delta_D \epsilon_a \epsilon_b)^{1/3}}\left\{\frac{3(1+z)m_e c^2\left(\epsilon_b^{1/2} - \epsilon_a^{1/2}\right)}{8c\sigma_{\rm T} u_{Bc}\Delta T}\right\}^{2/3}, \quad (70)$$

where $u_{Bc} = B_c^2/(8\pi)$. With $z = 0.03$ for Mrk 421 and $m_e c^2 \epsilon_a = 0.1$ keV and $m_e c^2 \epsilon_b = 2$ keV,

$$B = 0.7\left(\frac{\delta_{\rm D}}{30}\right)^{-1/3}\left(\frac{\Delta T}{10^3\ {\rm s}}\right)^{-2/3} \text{G}. \quad (71)$$

6.3. The Gamma-Ray PSDs of FSRQs and BL Lac Objects

Nakagawa & Mori (2013) used more than four years of *Fermi*-LAT data to compute the PSD of 15 blazars. Each PSD is fit with either a single or broken power-law model. Their values of b from their fits, where $S(\epsilon, f) \propto f^{-b}$ from the single power-law fit or lower index from the broken power-law fit if that fit is statistically significant are given in Table 1. We neglect the FSRQ S4 1030+61, which has poor statistics. There is a clear separation between b for FSRQs and BL Lac objects. All BL Lac objects have $b \leqslant 0.6$, while all FSRQs except for PKS 1222+216 have $b > 0.7$. PKS 1222+216 seems to be an outlier in terms of its PSD power-law index, although its b is still larger than for any of the BL Lac objects. We also compute the value of a from our model (recall its definition in Equation (14)) needed to reproduce the values of b. For FSRQs, presumably emitting by EC, this is just

$$a = b_{\rm EC},$$

while for BL Lac objects, presumably emitting by SSC, this is

$$a = \frac{b_{\rm SSC} + 2}{2}$$

Table 1
Fermi-LAT PSD Power-law Indices (b) from Nakagawa & Mori (2013) and the Values of a from Our Model Needed to Reproduce Them

Object	b	a
FSRQs		
4C +28.07	0.93 ± 0.23	0.93
PKS 0426−380[a]	1.16 ± 0.47	1.16
PKS 0454−234	0.78 ± 0.27	0.78
PKS 0537−441[a]	0.86 ± 0.64	0.86
PKS 1222+216	0.65 ± 0.21	0.65
3C 273	1.30 ± 0.27	1.30
3C 279	1.23 ± 0.35	1.23
PKS 1510−089	1.10 ± 0.30	1.10
3C 454.3	1.00 ± 0.24	1.00
PKS 2326−502	1.26 ± 0.44	1.26
Mean	1.01	1.01
S.D.	0.26	0.26
BL Lac Objects		
3C 66A	0.60 ± 0.44	1.22
Mrk 421	0.38 ± 0.21	1.19
PKS 2155−304	0.58 ± 0.33	1.29
BL Lac	0.41 ± 0.47	1.21
Mean	0.49	1.23
S.D.	0.11	0.07

Note. [a] PKS 0426−380 and PKS 0537−441 were previously classified as BL Lac objects.

(recall Section 5.2). The mean values of a for FSRQs and BL Lac objects are within one standard deviation (S.D.) of each other. The values of b from Nakagawa & Mori (2013) are in agreement with our theory with values of a that cluster around $a \sim 1$.

Based on the traditional classification, PKS 0537−441 and PKS 0426−380 are classified as BL Lac objects. However, based on the new classification by Ghisellini et al. (2011) they are considered FSRQs (see also Sbarrato et al. 2012). We use the more recent classification. For a discussion see D'Ammando et al. (2013) for PKS 0537−441 and Tanaka et al. (2013) for PKS 0426−380.

The PSD indices found by Nakagawa & Mori (2013) are in general not reproduced by an independent analysis by Sobolewska et al. (2014). This could be due to the different analysis techniques used by the different authors. More work is needed to resolve the discrepancies.

Ideally, to test our theory one would want simultaneous light curves from synchrotron emission (say, optical) and GeV γ-ray emission over a long timescale. The PSDs could be computed from these light curves. One expects that if the γ-rays are emitted by EC, they would have the same b as synchrotron ($b_{\rm sy} = b_{\rm EC} = a$). But if the γ-rays are produced by SSC emission, one would expect b to be less steep than for the γ-rays compared to the optical, with the relation between the SSC and synchrotron PSD indices given by $b_{\rm SSC} = 2b_{\rm sy} - 2 = 2a - 2$. Of course this could be complicated by emission from a thermal accretion disk unrelated to the jet emission.

6.4. The Gamma-Ray PSD of 3C 454.3

The PSD of 3C 454.3 from Nakagawa & Mori (2013) shows a break at frequency $f_{\rm brk} = 1.5 \times 10^{-6}$ Hz, corresponding to a timescale of 6.8×10^5 s $= 190$ hr $= 7.9$ days. Their broken power-law fit to the PSD, where $S(\epsilon, f) \propto f^{-b_1}$ at $f < f_{\rm brk}$

and $S(\epsilon, f) \propto f^{-b_2}$ at $f > f_{\rm brk}$, shows $b_1 \approx 1$ and $b_2 \approx 3$. This is a break of about 2, which is what is expected from our theory. The timescale could correspond to the light crossing, cooling, or escape timescales. If one interprets it as the light-crossing timescale, $t_{\rm lc}$, then

$$R' \approx \frac{c t_{\rm lc} \delta_{\rm D}}{2(1+z)} = 1.7 \times 10^{17} \left(\frac{\delta_{\rm D}}{30}\right) \ {\rm cm}. \quad (72)$$

Interpreting it as the cooling timescale, $t_{\rm cool}$, and assuming $\delta_{\rm D} = \Gamma$, the external radiation field is

$$\begin{aligned} u_0 \approx \frac{3 m_e c^2}{4 c \sigma_{\rm T} \Gamma^2 t'_{\rm cool} \gamma'} &= 9.6 \times 10^{-6} \left(\frac{\Gamma}{30}\right)^{-2} \left(\frac{E}{100 \ {\rm MeV}}\right)^{-1/2} \\ &\times \left(\frac{\epsilon_0}{5 \times 10^{-7}}\right)^{1/2} {\rm erg \ cm^{-3}} \\ &= 6.1 \times 10^{-5} \left(\frac{\Gamma}{30}\right)^{-2} \left(\frac{E}{100 \ {\rm MeV}}\right)^{-1/2} \\ &\times \left(\frac{\epsilon_0}{2 \times 10^{-5}}\right)^{1/2} {\rm erg \ cm^{-3}}, \end{aligned} \quad (73)$$

where E is the observed photon energy. The first line assumes the seed photon source is a dust torus with temperature 1000 K; the second assumes it is Lyα, presumably from the broad-line region. Both numbers give rather low values for u_0.

However, interpreting the break as either the cooling timescale or the light crossing timescale is problematic, since variations on timescales much shorter than this have been observed from 3C 454.3, including decreases on much faster timescales (Ackermann et al. 2010; Abdo et al. 2011a). But one could also associate the break with the escape timescale for electrons in the blob, as shown in Section 5.1. This break will occur at $f = (2\pi t_{\rm esc})^{-1}$, so if $t_{\rm lc} = t_{\rm esc}$, the break will still be at a frequency 2π lower than the one related to the light crossing timescale. Furthermore, the escape timescale could in principle be longer than the light crossing timescale, since magnetic fields in the blob would curve the electron's path and decrease the time it takes to escape. We note that in Figure 4, the break in the 0.1 GeV PSD is indeed associated with the escape timescale, $f = (2\pi t_{\rm esc})^{-1}$, showing that this is at least plausible. If the break in the PSD of 3C 454.3 (Nakagawa & Mori 2013) is due to electron escape, then the escape timescale in the observer's frame will be $t_{\rm esc} = 7.9 \ {\rm days}/(2\pi) = 30$ hr, and in the comoving frame,

$$t'_{\rm esc} = 20 \ {\rm days} \left(\frac{\delta_D}{30}\right). \quad (74)$$

How could one distinguish between these interpretations? One possibility would be to observe the PSDs at more than one waveband. If the break is due to the light-crossing timescale, the break frequency should be present independent of the waveband. The escape timescale break could also be independent of frequency if the escape timescale is energy independent, as it is in our model. The cooling timescale should be energy-dependent, and thus the break frequency will be different in different wavebands. For 3C 454.3, the light-crossing timescale interpretation is disfavored since smaller timescale fluctuations are present in its light curve (e.g., Ackermann et al. 2010; Abdo et al. 2011a).

6.5. Optical PSDs of Blazars

Chatterjee et al. (2012) compute R band PSDs for 6 blazars based on about 200–250 days of continuous data. Their PSDs have power-law indices that are significantly steeper than those from the same objects' γ-ray PSDs from Nakagawa & Mori (2013). The exception is PKS 1510−089, for which Chatterjee et al. (2012) compute $b = 0.6^{+0.2}_{-0.5}$, significantly flatter than the γ-ray PSD. Our theory predicts that synchrotron and EC emission should have the same PSD slopes if produced by the same electron energies, and all but one of their sources are FSRQs, which are expected to emit γ-rays by EC. One possible reason for the discrepancy could be the contamination in the optical by the accretion disk. Another possibility is that the time intervals used by Chatterjee et al. (2012) are significantly shorter than the ones used by Nakagawa & Mori (2013). As Chatterjee et al. (2012) point out, the large number of bright flares in their time interval for PKS 1510−089 could be the cause of its especially flat R band PSD power-law index. It could also be that the different analysis methods used by Chatterjee et al. (2012) and Nakagawa & Mori (2013) could lead to different results. Finally, it could be that one of the assumptions of our theory is just not correct.

The *Kepler* mission, with its excellent relative photometry and short timescale sampling is well-suited for measuring high-frequency PSDs. Wehrle et al. (2013) reported the *Kepler* PSDs of several radio-loud AGNs, and found no departure from a single power law up to $\sim 10^{-5}$ Hz, above which white noise dominates. Edelson et al. (2013) explored the *Kepler* PSD of the BL Lac object W2R1926+42 and found a "bending" power law provided a good fit to its PSD, with "bend frequency" corresponding to ≈4 hr. The source W2R1926+42 has a synchrotron peak at $10^{14.5}$ Hz according to Edelson et al. (2013), making it an intermediate synchrotron peaked object by the classification of Abdo et al. (2010a). However, its optical SED appears to be dominated by accretion disk emission, implying its synchrotron peak is probably at $\lesssim 10^{13.5}$ Hz, which would make it a low-synchrotron peaked (LSP). The *Kepler* light curve could have a contribution from both the thermal accretion disk emission and the nonthermal jet emission, making interpretation of its PSD difficult. If the optical band is dominated by synchrotron emission, its status as an LSP implies that the electrons that produce its optical emission are in the regime $\gamma' \gg (\nu t'_{\rm esc})^{-1}$, meaning the "bend frequency" could be associated with the light-crossing timescale or the cooling timescale. If it is associated with the light-crossing timescale, the size of the emitting region is

$$R' \approx 5.5 \times 10^{15} \left(\frac{\delta_{\rm D}}{30}\right) \ {\rm cm}. \quad (75)$$

If it is associated with the cooling timescale, the cooling is dominated by EC, and $\delta_{\rm D} = \Gamma$, then

$$\begin{aligned} u_0 \approx 3.2 \times 10^{-5} &\left(\frac{\Gamma}{30}\right)^{-5/2} \left(\frac{B}{1 \ {\rm G}}\right)^{1/2} \\ &\times \left(\frac{\lambda_{\rm obs}}{5000 \ {\rm \AA}}\right)^{-1/2} {\rm erg \ cm^{-3}}, \end{aligned} \quad (76)$$

where $\lambda_{\rm obs}$ is the observed wavelength. If the cooling is dominated by synchrotron, then the cooling timescale can be used to estimate the magnetic field,

$$B \approx 0.81 \left(\frac{\delta_{\rm D}}{30}\right)^{-1/3} \left(\frac{\lambda_{\rm obs}}{5000 \ {\rm \AA}}\right)^{-1/3} {\rm G}. \quad (77)$$

6.6. The X-Ray PSD of 3C 273

An X-ray PSD of 3C 273 based on data combined from *RXTE*, *EXOSAT*, and other instruments was reported by McHardy (2008). Similar to the γ-ray PSD of 3C 454.3, the PSD shows two power laws with $b_1 \approx 1.1$, $b_2 \approx 2.9$, with $f_{\rm brk} \approx 1.0 \times 10^{-6}$ Hz. The break is close to 2, and the break frequency corresponds to a timescale of 1.0×10^6 s ≈ 280 hr $\approx$12 days. The interpretation for this break is more difficult than the γ-ray PSD for 3C 454.3, since it is not clear whether the X-rays are produced by SSC, EC, or even by a hot corona at the base of the jet. If the X-ray emission is dominated by EC, the most likely interpretation of the break is with the escape timescale, since the electrons generating the EC emission will almost certainly have Lorentz factors $\gamma \ll (\nu t_{\rm esc})^{-1}$. In this case the escape timescale in the observer's frame is $t_{\rm esc} = 12$ days$/(2\pi) = 46$ hr.

6.7. Quasi-periodic Oscillations

A number of quasi-periodic oscillations (QPOs) have been reported in the X-ray and optical PSDs of blazars. These QPOs could be associated with the maxima at half-integer values of either the light crossing timescale ($t_{\rm lc}$) or the cooling timescale ($t_{\rm cool}$). See for example Figure 4, where maxima in the 0.648 μm or 1.0 GeV PSDs could be confused with QPOs in noisy PSDs. If this interpretation is correct, one could distinguish between these possibilities ($t_{\rm lc}$ or $t_{\rm cool}$) by observing the PSDs at more than one wavelength. If the QPO appears at the same frequency independent of wavelength, it would argue for a $t_{\rm lc}$ interpretation. If QPOs are found at different frequencies at different wavelengths, it argues for the $t_{\rm cool}$ interpretation. Assessing the significance of QPOs in red noise PSDs can be subtle (e.g., Vaughan 2005; Vaughan & Uttley 2006).

As an example, we look at the claimed QPO reported in *XMM-Newton* observations of PKS 2155−304 (Lachowicz et al. 2009). Visually inspecting their PSD from data taken between 0.3 and 10 keV, one sees significant maxima at $\sim 3.5 \times 10^{-5}$ Hz and $\sim 7.0 \times 10^{-5}$ Hz. Lachowicz et al. (2009) also examined the PSDs in the energy bands 0.3–2 keV and 2–10 keV, and found the maxima were significant in the soft band but not in the hard band, although they were still found in the hard band. Gaur et al. (2010) and González-Martín & Vaughan (2012) find this QPO in only one of many *XMM-Newton* observations of this source. If the maxima are significant and found in both energy bands, this argues for a light crossing time interpretation, with timescale $t_{\rm lc} = 3.8 \times 10^4$ s and

$$R' \approx \frac{c t_{\rm lc} \delta_{\rm D}}{2(1+z)} = 3.1 \times 10^{16} \left(\frac{\delta_{\rm D}}{60}\right) \text{ cm}. \quad (78)$$

This is larger than the size from the HESS observation (Section 6.1). The *XMM-Newton* observations were taken on 2006 May 1, and the HESS observations on 2006 July 28, which could account for the discrepancy. The emitting region size could have been different at different times. A number of claimed significant detections of QPOs from the literature are listed in Table 2.

Table 2
Claimed QPOs from Blazars Reported in the Literature

Authors	Object	Bandpass	QPO Frequency (Hz)
Espaillat et al. (2008)[a]	3C 273	0.75–10 keV	3.0×10^{-4}
Lachowicz et al. (2009)	PKS 2155−304	0.2–10 keV	6×10^{-5}
Gupta et al. (2009)	S5 0716+714	*V* and *R* band	Various
Rani et al. (2010)	S5 0716+714	*R* band	1.1×10^{-3}

Note. [a] This claimed QPO is disputed by Mohan et al. (2011) and González-Martín & Vaughan (2012).

7. DISCUSSION

We have presented a new theoretical formalism for modeling the variability of blazars, based on an analytical solution to the underlying electron continuity equation governing the distribution of radiating electrons in a homogeneous blob moving out in the jet. The analysis was carried out in the Fourier domain, and the results are therefore directly comparable with observational Fourier data products such as the PSDs and time/phase lags. This formalism assumes emission from a jet closely aligned with the line of sight, so that the emission produced in the comoving frame is Doppler shifted into the observer's frame. Internal shocks in the jet randomly accelerate electrons to high energies, which are then injected into an emitting region at random intervals with that variability characterized by a power law in Fourier space. The observable radiation produced by the electrons is affected by cooling, electron escape, and the light-travel time across the blob. The model makes specific predictions regarding the PSDs and Fourier-dependent time lag components resulting from synchrotron, EC, and SSC emission, and it successfully reproduces the characteristics of the colored noise seen in nearly all blazars.

The study presented here is a first attempt at examining blazar variability with this formalism. As such, it makes a number of simplifying assumptions.

1. It assumes the only thing which varies with time in a blazar is the rate at which electrons are injected into the emitting region. All other parameters—the magnetic field strength (B), the size of the emitting region (R'), the electron injection power-law index (q), the jet's angle to the line of sight (θ), and so on—are assumed not to vary. Although this is likely an over-simplification, we note that the PSDs of PKS 0537−441 can be explained by only varying the electron distribution of the source (D'Ammando et al. 2013), so that in some cases this may be justified.
2. In computing emission, we have used simplified δ-function expressions for the synchrotron and Compton emission, and assumed Thomson scattering. Using more accurate expressions, in particular, the full Compton cross-section for the energy losses could lead to interesting effects (Dermer & Atoyan 2002; Moderski et al. 2005; Sikora et al. 2009; Dotson et al. 2012).
3. The calculations neglect SSC cooling, which is quite difficult to model analytically (Schlickeiser 2009; Zacharias & Schlickeiser 2010, 2012a, 2012b). This would likely not be important for FSRQs, where the EC component probably dominates the cooling, but could be important for BL Lac objects that do not have a strong external radiation field.
4. We have neglected the details of the acceleration mechanism. Such a mechanism may produce interesting features in PSDs that could be observable.
5. Although we take light travel-time effects into account, we assume all parts of the blob vary simultaneously, which is obviously not the case.

In the future, we will perform more detailed analyses which explore these more complicated cases.

What are the best wavebands to observe blazars and compare with the theory outlined in this work? Observations at (electromagnetic) frequencies lower than $\sim 10^{12}$ Hz would not be useful, since here the emission is likely dominated by the superposition of many self-absorbed jet components (Konigl 1981). For LSP blazars (including almost all FSRQs; Finke 2013), The optical and GeV γ-rays would have features at high Fourier frequencies due the rapid energy losses of electrons that produce this radiation, and thus this emission could be quite interesting to observe. Observing such short timescales with the *Fermi*-LAT could be difficult, since for this instrument one must usually integrate over fairly long timescales ($\gtrsim$a few hours for all but the brightest sources) to get a significant detection. Bright flares and adaptive light curve binning may be helpful in producing accurate LAT PSDs at high Fourier frequencies (Lott et al. 2012). Significant detections can be made in the optical with shorter integration times ($\sim$ a few minutes or even fractions of a minute), leading to better PSDs at high frequencies (e.g., Rani et al. 2010), although in FSRQs this could be contaminated by thermal emission from an accretion disk.

Observing LSPs at wavebands (e.g., infrared) where emission is dominated by less energetic electrons could probe the escape timescale. PSDs produced from simultaneous light curves at multiple frequencies would be extremely helpful for verifying the predictions of this paper. At low Fourier frequencies the PSDs should have essentially identical power-law shapes at all wavebands, and at higher Fourier frequencies features associated with the light-crossing timescale could be identified, and should be the same in all wavebands. This could serve as a strong test for the theory presented in this paper. We also predict that all breaks in observed synchrotron and EC PSD power laws should be by 2, i.e., from $\propto f^{-a}$ to $\propto f^{-(a+2)}$, and more gradual breaks could be observed in SSC PSDs. Kataoka et al. (2001) observed smaller breaks in the X-ray PSDs of Mrk 421, Mrk 501, and PKS 2155−304 based on *ASCA* and *Rossi X-ray Timing Explorer* observations. However, note that they did not obtain acceptable fits to their PSDs with broken power laws with all parameters left free to vary. Also, it may be that including SSC cooling could modify the PSD so that breaks other than 2 are possible, although that is beyond the scope of this paper.

For high synchrotron-peaked blazars (HSPs), almost all of which are BL Lac objects, the γ-ray emission is expected to be from SSC. We do not predict any features in SSC PSDs from cooling or escape, although features from the light crossing time are still expected. These predictions could be tested with *Fermi*-LAT and VHE γ-ray instruments such as MAGIC, HESS, VERITAS, and the upcoming CTA. For synchrotron emission, however, features from cooling and escape should be present. An X-ray telescope could be used to probe emission from the highest energy electrons potentially seeing cooling features. The proposed *Large Observatory for X-ray Timing* (*LOFT*) spacecraft could be very useful for this (Donnarumma et al. 2013). *LOFT* will provide excellent timing coverage ($\sim$ ms) with a relatively large effective area. PSDs produced from optical light curves of HSPs could be used to probe the escape timescale. As with LSP blazars, PSDs produced by simultaneous light curves from multiple wavebands would be extremely helpful for the study of HSP blazars.

We are grateful to the anonymous referee for insightful suggestions that helped improve the discussion and presentation, and to C. Dermer for useful discussions. J.D.F. was supported by the Office of Naval Research.

APPENDIX A

SOLUTION TO THE FOURIER TRANSFORM OF THE CONTINUITY EQUATION

Here we solve the differential equation

$$-2\pi i f \tilde{N}_e(\gamma, f) + \frac{\partial}{\partial\gamma}[\dot{\gamma}(\gamma)\tilde{N}_e(\gamma, f)] + \frac{\tilde{N}_e(\gamma, f)}{t_{\rm esc}(\gamma)} = \tilde{Q}(\gamma; f) \quad \text{(A1)}$$

for $\dot{\gamma} \leqslant 0$. This equation can be rearranged,

$$\frac{\partial}{\partial\gamma}[\dot{\gamma}(\gamma)\tilde{N}_e(\gamma, f)] + \left[\frac{1}{t_{\rm esc}} - i\omega\right]\tilde{N}_e(\gamma, f) = \tilde{Q}(\gamma; f), \quad \text{(A2)}$$

recalling that $\omega = 2\pi f$. One can multiply both sides by

$$\exp\left[\int_\gamma^\infty \frac{d\gamma'}{|\dot{\gamma}(\gamma')|}\left(\frac{1}{t_{\rm esc}} - i\omega\right)\right] \quad \text{(A3)}$$

and then rearrange the left side so that

$$\frac{d}{d\gamma}\left\{\dot{\gamma}(\gamma)\tilde{N}_e(\gamma, f)\exp\left[\int_\gamma^\infty \frac{d\gamma'}{|\dot{\gamma}(\gamma')|}\left(\frac{1}{t_{\rm esc}} - i\omega\right)\right]\right\} = \tilde{Q}(\gamma; f)\exp\left[\int_\gamma^\infty \frac{d\gamma'}{|\dot{\gamma}(\gamma')|}\left(\frac{1}{t_{\rm esc}} - i\omega\right)\right]. \quad \text{(A4)}$$

Integrating both sides gives

$$|\dot{\gamma}(\gamma)|\tilde{N}_e(\gamma, f)\exp\left[\int_\gamma^\infty \frac{d\gamma'}{|\dot{\gamma}(\gamma')|}\left(\frac{1}{t_{\rm esc}} - i\omega\right)\right] = \int_\gamma^\infty d\gamma'\ \tilde{Q}(\gamma'; f)\exp\left[\int_{\gamma'}^\infty \frac{d\gamma''}{|\dot{\gamma}(\gamma'')|}\left(\frac{1}{t_{\rm esc}} - i\omega\right)\right]. \quad \text{(A5)}$$

Solving this for $\tilde{N}(\gamma, f)$ results in

$$\tilde{N}_e(\gamma, f) = \frac{1}{|\dot{\gamma}(\gamma)|}\int_\gamma^\infty d\gamma'\ \tilde{Q}(\gamma'; f) \times \exp\left[-\int_\gamma^{\gamma'} \frac{d\gamma''}{|\dot{\gamma}(\gamma'')|}\left(\frac{1}{t_{\rm esc}(\gamma'')} - i\omega\right)\right]. \quad \text{(A6)}$$

APPENDIX B

NORMALIZATION OF ELECTRON INJECTION FUNCTION

The time average of the total power injected in electrons is

$$\langle L_{\rm inj}\rangle = \frac{m_e c^2}{\Delta t}\int_1^\infty d\gamma\ \gamma \int_0^{\Delta t} dt\ Q(\gamma, t), \quad \text{(B1)}$$

where Δt is the length of the time interval over which the electrons are injected. Using Equation (2),

$$\langle L_{\rm inj}\rangle = \frac{m_e c^2}{\Delta t}\int_1^\infty d\gamma\ \gamma \int_{-\infty}^\infty df\ \tilde{Q}(\gamma, f) \times \int_0^{\Delta t} dt\ \exp[-2\pi i f t]. \quad \text{(B2)}$$

Substituting Equation (14),

$$\tilde{Q}(\gamma;\, f) = Q_0 (f/f_0)^{-a/2} \gamma^{-q} H(\gamma;\, \gamma_1,\, \gamma_2) \times H(f;\, f_1,\, f_2), \quad \text{(B3)}$$

and integrating over γ, one gets

$$\langle L_{\rm inj} \rangle = \frac{m_e c^2}{\Delta t} Q_0\, G(q,\, \gamma_1,\, \gamma_2) \int_{f_1}^{f_2} df\, (f/f_0)^{-a/2} \times \int_0^{\Delta t} dt\, \exp[-2\pi i f t], \quad \text{(B4)}$$

where

$$G(q,\, \gamma_1,\, \gamma_2) = \begin{cases} \left(\gamma_1^{2-q} - \gamma_2^{2-q}\right)/(q-2) & \text{for } q \neq 2 \\ \ln(\gamma_2/\gamma_1) & \text{for } q = 2 \end{cases}. \quad \text{(B5)}$$

Performing the integral over time gives

$$\langle L_{\rm inj} \rangle = \frac{m_e c^2}{-2\pi i \Delta t} Q_0\, G(q,\, \gamma_1,\, \gamma_2) \int_{f_1}^{f_2} \frac{df}{f} (f/f_0)^{-a/2} \times [\exp(-2\pi i f \Delta t) - 1]. \quad \text{(B6)}$$

This can be rewritten as

$$\langle L_{\rm inj} \rangle = \frac{m_e c^2}{-2\pi i \Delta t} Q_0\, G(q,\, \gamma_1,\, \gamma_2)\, [I_r(a,\, f_1,\, f_2) - i\, I_i(a,\, f_1,\, f_2) - I_0(a,\, f_1,\, f_2)], \quad \text{(B7)}$$

where

$$I_r(a,\, f_1,\, f_2) = \int_{f_1}^{f_2} \frac{df}{f} (f/f_0)^{-a/2} \cos(2\pi f \Delta t), \quad \text{(B8)}$$

$$I_i(a,\, f_1,\, f_2) = \int_{f_1}^{f_2} \frac{df}{f} (f/f_0)^{-a/2} \sin(2\pi f \Delta t), \quad \text{(B9)}$$

and

$$I_0(a,\, f_1,\, f_2) = \int_{f_1}^{f_2} \frac{df}{f} (f/f_0)^{-a/2} = \begin{cases} 2/a[(f_1/f_0)^{-a/2} - (f_2/f_0)^{-a/2}] & a \neq 0 \\ \ln(f_2/f_1) & a = 0 \end{cases}. \quad \text{(B10)}$$

Multiplying Equation (B7) by its complex conjugate gives

$$|\langle L_{\rm inj} \rangle|^2 = \left[\frac{m_e c^2 Q_0 G}{2\pi \Delta t}\right]^2 \left[I_r^2 + I_i^2 - 2 I_r I_0 + I_0^2\right], \quad \text{(B11)}$$

or, solving for Q_0,

$$Q_0 = \frac{2\pi \Delta t \langle L_{\rm inj} \rangle}{m_e c^2 G \sqrt{I_r^2 + I_i^2 - 2 I_r I_0 + I_0^2}}. \quad \text{(B12)}$$

APPENDIX C
LIGHT TRAVEL TIME

Let us take a cylindrical blob, as shown in cross section in Figure 8. The blob has length $2R$, and everywhere within the blob radiation is emitted simultaneously as a function of time t as $g(t)$. The entire blob has length $2R$ and is divided into N individual segments, each with length $\Delta x = 2R/N$. The radiation emitted by each individual segment is a corresponding fraction of the whole, $g(t)/N = g(t)\Delta x/2R$. The radiation an observer co-moving with the blob sees at any given time $t_{\rm obs}$ will be a sum over the individual segments at that time,

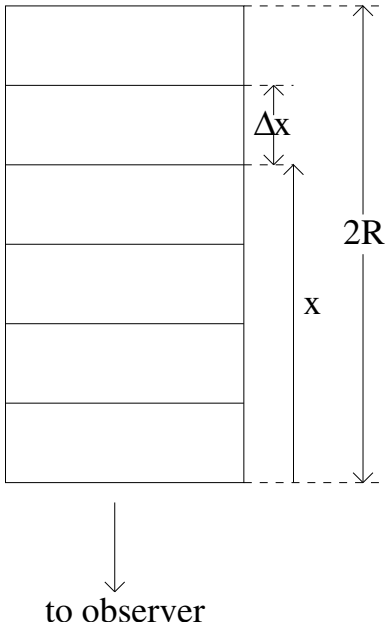

Figure 8. Sketch of the geometry of the emitting blob for the purpose of computing light travel time effects. This sketch is in the frame co-moving with the blob. The blob of length $2R$ is divided into N pieces each with length Δx.

$$h(t_{\rm obs}) = g(t_{\rm obs} - x_1/c)\, \Delta x/(2R) + g(t_{\rm obs} - x_2/c)\, \Delta x/(2R) + \ldots + g(t_{\rm obs} - 2R/c)\, \Delta x/(2R) \quad \text{(C1)}$$

or

$$h(t_{\rm obs}) = \frac{1}{2R} \sum_{j=1}^{N} g(t_{\rm obs} - x_j/c)\, \Delta x. \quad \text{(C2)}$$

As $N \to \infty$,

$$h(t_{\rm obs}) \to \frac{1}{2R} \int_0^{2R} dx\, g(t_{\rm obs} - x/c). \quad \text{(C3)}$$

Since $t = x/c$,

$$h(t_{\rm obs}) = \frac{c}{2R} \int_0^{2R/c} dt\, g(t_{\rm obs} - t). \quad \text{(C4)}$$

Let us now move to a frame where the blob is moving relative to the observer so that she or he sees a time $t_{\rm obs} = t'_{\rm obs}(1+z)/\delta_{\rm D}$, where now all lengths and times in the co-moving frame will be primed. Then

$$h(t_{\rm obs}) = \frac{c}{2R'} \int_0^{2R'/c} dt'\, g(t'_{\rm obs} - t') = \frac{c}{2R'} \int_0^{2R'/c} dt'\, g\left(\frac{t_{\rm obs}\delta_{\rm D}}{1+z} - t'\right). \quad \text{(C5)}$$

This is similar to the "time slices" of Chiaberge & Ghisellini (1999). We use a cylindrical normal blob geometry for simplicity

here, although a spherical one would be more consistent with the SSC calculation. Since the actual geometry of an emitting blob is not known, differences should not be too great. A similar derivation for a spherical geometry is given by Zacharias & Schlickeiser (2013).

APPENDIX D

FOURIER TRANSFORM INCLUDING LIGHT TRAVEL TIME

In this appendix we derive Equation (47) from Equation (40). From the definition of the inverse Fourier transform, Equation (2),

$$N_e(\gamma; t) = \int_{-\infty}^{\infty} df\, \tilde{N}_e(\gamma, f) \exp(-2\pi i f t). \quad \text{(D1)}$$

Putting this in Equation (40) and rearranging gives

$$F_\epsilon(t) = \frac{K(1+z)}{t_{\rm lc}\delta_{\rm D}} \int_{-\infty}^{\infty} df' \tilde{N}_e(\gamma', f') \times \exp\left[-\frac{2\pi i f' \delta_D t}{1+z}\right] \int_0^{2R'/c} dt' \exp(2\pi i f' t'), \quad \text{(D2)}$$

recalling that $t_{\rm lc} = 2R'(1+z)/(c\delta_{\rm D})$. Performing the integral over t' gives

$$F_\epsilon(t) = \frac{K(1+z)}{2\pi i t_{\rm lc}\delta_{\rm D}} \int_{-\infty}^{\infty} \frac{df'}{f'} \tilde{N}_e(\gamma', f') \exp\left[\frac{-2\pi i f' \delta_{\rm D} t}{1+z}\right] \times \left\{\exp\left[\frac{4\pi i f' R'}{c}\right] - 1\right\}. \quad \text{(D3)}$$

The Fourier transform of the synchrotron flux light curve is defined as (see Equation (1))

$$\tilde{F}_\epsilon(f) = \int_{-\infty}^{\infty} dt\ F_\epsilon(t) \exp(2\pi i f t). \quad \text{(D4)}$$

Substituting Equation (D3) for $F_\epsilon(t)$ in this equation gives

$$\tilde{F}_\epsilon(f) = \frac{K(1+z)}{2\pi i t_{\rm lc}\delta_{\rm D}} \int_{-\infty}^{\infty} \frac{df'}{f'} \tilde{N}_e(\gamma', f') \left\{\exp\left[\frac{4\pi i f' R'}{c}\right] - 1\right\} \times \int_{-\infty}^{\infty} dt \exp\left[2\pi i t \left(f - \frac{f'\delta_{\rm D}}{1+z}\right)\right]. \quad \text{(D5)}$$

The integral over t has the form of a Dirac δ-function (Equation (4)), so

$$\tilde{F}_\epsilon(f) = \frac{K(1+z)}{2\pi i t_{\rm lc}\delta_{\rm D}} \int_{-\infty}^{\infty} \frac{df'}{f'} \tilde{N}_e(\gamma', f') \times \left\{\exp\left[\frac{4\pi i f' R'}{c}\right] - 1\right\} \delta\left(f - \frac{f'\delta_{\rm D}}{1+z}\right). \quad \text{(D6)}$$

Using the well-known property for δ functions,

$$\delta\left(f - \frac{f'\delta_{\rm D}}{1+z}\right) = \frac{1+z}{\delta_{\rm D}} \delta\left(f' - \frac{(1+z)f}{\delta_{\rm D}}\right), \quad \text{(D7)}$$

one can perform the integral over f' in Equation (D6) to get

$$\tilde{F}_\epsilon(f) = \frac{K(1+z)}{2\pi i f t_{\rm lc}\delta_{\rm D}} \tilde{N}_e\left(\gamma', \frac{(1+z)f}{\delta_{\rm D}}\right) \times \left\{\exp\left[\frac{4\pi i f (1+z) R'}{c\delta_{\rm D}}\right] - 1\right\}. \quad \text{(D8)}$$

This is Equation (47).

REFERENCES

Abdo, A. A., Ackermann, M., Agudo, I., et al. 2010a, ApJ, 716, 30
Abdo, A. A., Ackermann, M., Ajello, M., et al. 2010b, ApJS, 188, 405
Abdo, A. A., Ackermann, M., Ajello, M., et al. 2010c, ApJ, 722, 520
Abdo, A. A., Ackermann, M., Ajello, M., et al. 2011a, ApJL, 733, L26
Abdo, A. A., Ackermann, M., Ajello, M., et al. 2011b, ApJ, 736, 131
Abdo, A. A., Ackermann, M., Ajello, M., et al. 2011c, ApJ, 727, 129
Ackermann, M., Ajello, M., Baldini, L., et al. 2010, ApJ, 721, 1383
Aharonian, F., Akhperjanian, A. G., Bazer-Bachi, A. R., et al. 2007, ApJL, 664, L71
Begelman, M. C., Fabian, A. C., & Rees, M. J. 2008, MNRAS, 384, L19
Błażejowski, M., Sikora, M., Moderski, R., & Madejski, G. M. 2000, ApJ, 545, 107
Bloom, S. D., & Marscher, A. P. 1996, ApJ, 461, 657
Böttcher, M., & Chiang, J. 2002, ApJ, 581, 127
Böttcher, M., & Reimer, A. 2004, ApJ, 609, 576
Chatterjee, R., Bailyn, C. D., Bonning, E. W., et al. 2012, ApJ, 749, 191
Chen, X., Fossati, G., Böttcher, M., & Liang, E. 2012, MNRAS, 424, 789
Chen, X., Fossati, G., Liang, E. P., & Böttcher, M. 2011, MNRAS, 416, 2368
Chiaberge, M., & Ghisellini, G. 1999, MNRAS, 306, 551
Cui, W. 2004, ApJ, 605, 662
D'Ammando, F., Antolini, E., Tosti, G., et al. 2013, MNRAS, 431, 2481
Dermer, C. D., & Atoyan, A. M. 2002, ApJL, 568, L81
Dermer, C. D., & Menon, G. 2009, High Energy Radiation from Black Holes: Gamma Rays, Cosmic Rays, and Neutrinos (Princeton, NJ: Princeton Univ. Press)
Dermer, C. D., & Schlickeiser, R. 1993, ApJ, 416, 458
Dermer, C. D., & Schlickeiser, R. 2002, ApJ, 575, 667
Donnarumma, I., Tramacere, A., Turriziani, S., et al. 2013, EPJWC, 61, 4015
Dotson, A., Georganopoulos, M., Kazanas, D., & Perlman, E. S. 2012, ApJL, 758, L15
Edelson, R., Mushotzky, R., Vaughan, S., et al. 2013, ApJ, 766, 16
Espaillat, C., Bregman, J., Hughes, P., & Lloyd-Davies, E. 2008, ApJ, 679, 182
Finke, J. D. 2013, ApJ, 763, 134
Finke, J. D., Dermer, C. D., & Böttcher, M. 2008, ApJ, 686, 181
Gaur, H., Gupta, A. C., Lachowicz, P., & Wiita, P. J. 2010, ApJ, 718, 279
Ghisellini, G., Tavecchio, F., Foschini, L., & Ghirlanda, G. 2011, MNRAS, 414, 2674
González-Martín, O., & Vaughan, S. 2012, A&A, 544, A80
Gupta, A. C., Srivastava, A. K., & Wiita, P. J. 2009, ApJ, 690, 216
Hayashida, M., Madejski, G. M., Nalewajko, K., et al. 2012, ApJ, 754, 114
Joshi, M., & Böttcher, M. 2007, ApJ, 662, 884
Kataoka, J., Mattox, J. R., Quinn, J., et al. 1999, ApJ, 514, 138
Kataoka, J., Takahashi, T., Wagner, S. J., et al. 2001, ApJ, 560, 659
Konigl, A. 1981, ApJ, 243, 700
Kroon, J. J., & Becker, P. A. 2014, ApJL, 785, L34
Lachowicz, P., Gupta, A. C., Gaur, H., & Wiita, P. J. 2009, A&A, 506, L17
Li, H., & Kusunose, M. 2000, ApJ, 536, 729
Lott, B., Escande, L., Larsson, S., & Ballet, J. 2012, A&A, 544, A6
Malmrose, M. P., Marscher, A. P., Jorstad, S. G., Nikutta, R., & Elitzur, M. 2011, ApJ, 732, 116
Mastichiadis, A., Petropoulou, M., & Dimitrakoudis, S. 2013, MNRAS, 434, 2684
McHardy, I. 2008, Proc. Blazar Variability across the Electromagnetic Spectrum, PoS (BLAZARS2008) (Trieste: SISSA Proc. Sci), 14
Moderski, R., Sikora, M., Coppi, P. S., & Aharonian, F. 2005, MNRAS, 363, 954
Mohan, P., Mangalam, A., Chand, H., & Gupta, A. C. 2011, JApA, 32, 117
Nakagawa, K., & Mori, M. 2013, ApJ, 773, 177
Nolan, P. L., Abdo, A. A., Ackermann, M., et al. 2012, ApJS, 199, 31
Rani, B., Gupta, A. C., Joshi, U. C., Ganesh, S., & Wiita, P. J. 2010, ApJL, 719, L153
Sbarrato, T., Ghisellini, G., Maraschi, L., & Colpi, M. 2012, MNRAS, 421, 1764
Schlickeiser, R. 2009, MNRAS, 398, 1483
Schlickeiser, R., Böttcher, M., & Menzler, U. 2010, A&A, 519, A9
Sikora, M., Begelman, M. C., & Rees, M. J. 1994, ApJ, 421, 153
Sikora, M., Stawarz, Ł., Moderski, R., Nalewajko, K., & Madejski, G. M. 2009, ApJ, 704, 38
Sobolewska, M. A., Siemiginowska, A., Kelly, B. C., & Nalewajko, K. 2014, ApJ, 786, 143
Tanaka, Y. T., Cheung, C. C., Inoue, Y., et al. 2013, ApJL, 777, L18

Vaughan, S. 2005, A&A, 431, 391
Vaughan, S., & Uttley, P. 2006, AdSpR, 38, 1405
Wehrle, A. E., Wiita, P. J., Unwin, S. C., et al. 2013, ApJ, 773, 89
Zacharias, M., & Schlickeiser, R. 2010, A&A, 524, A31
Zacharias, M., & Schlickeiser, R. 2012a, MNRAS, 420, 84
Zacharias, M., & Schlickeiser, R. 2012b, ApJ, 761, 110
Zacharias, M., & Schlickeiser, R. 2013, ApJ, 777, 109
Zhang, Y. H. 2002, MNRAS, 337, 609
Zhang, Y. H., Celotti, A., Treves, A., et al. 1999, ApJ, 527, 719
Zhang, Y. H., Treves, A., Celotti, A., et al. 2002, ApJ, 572, 762